ARCHIVES OF MECHANICS
Arch. Mech. **75** (5), 591–616, 2023, DOI: 10.24423/aom.4353

# Prediction of laminar-to-turbulent transition in a separated boundary layer subjected to an external acoustic forcing

S. KUBACKI[1*)], Z. RARATA[1)], A. DRÓŻDŻ[2)], R. GNATOWSKA[2)], V. SOKOLENKO[2)], W. ELSNER [2)]

[1)] *Warsaw University of Technology, Faculty of Power and Aeronautical Engineering, Institute of Aeronautics and Applied Mechanics, Nowowiejska 24, 00-665, Warsaw, Poland,* [*)] *e-mail: Slawomir.Kubacki@pw.edu.pl (corresponding author)*

[2)] *Częstochowa University of Technology, Armii Krajowej 21, 42-200, Częstochowa, Poland*

The new Reynolds-averaged Navier–Stokes (RANS)-based method has been developed for taking into account, in an approximate manner, the effect of external acoustic forcing on laminar-to-turbulent transition in a separated boundary layer. Experimental studies [33] report an increase of the turbulent shear stress within the separated boundary layer under the influence of acoustic forcing. Enhancement of flow disturbances in a reversed flow region was also reported in our experiment. Experimental findings stimulated the development of a reduced-order aero-acoustic strategy. The effect of acoustic forcing was incorporated into the modelling framework of an algebraic intermittency model. The model component was tuned based on our experimental data and validated on reference experiments. The results show the feasibility of the proposed model to simulate flow over a flat plate and the NACA0018 profile.

**Key words:** laminar-to-turbulent transition, separated boundary layer, acoustic excitation, algebraic intermittency model.

## 1. Introduction

An aerodynamic shape optimization is commonly carried out with the application of Reynolds-averaged Navier–Stokes techniques. Although many flows have been accurately predicted using the RANS approach, there are topics such as influence of acoustic waves on boundary layer flow which can only be simulated by applying high-fidelity Direct Numerical Simulation (DNS) or Large Eddy Simulation (LES) techniques. An application of high-fidelity eddy-resolving strategies is prohibitively expensive and is not feasible in the design process of aircraft components. Thus, the capabilities of RANS techniques have to be developed to properly address a possible effect of external acoustic forcing on the development of the boundary layers on aerodynamic surfaces, such as wings or turbomachinery blades.

As stressed in NASA Vision 2030 [1], multidisciplinary design and optimization strategies based on aero-acoustic simulation capabilities must be ready in the near future. A goal of achieving net-zero carbon emission by air transport by 2050 forces the development of reliable and cost-effective design strategies, which should be supported with reliable Computational Fluid Dynamics (CFD) tools. RANS models are workhorses of applied CFD, but they still suffer from difficulties in the prediction of profile losses due to transitional boundary layers. Thus further improvement of the predictive qualities of RANS models is needed to cope with the abovementioned challenges. Efforts have been made in the present work to develop the RANS-based method for taking into account the effect of external acoustic forcing on transition in a separated boundary layer.

The separated flow physics was investigated by means of DNS, LES and experiments. MCAULIFFE and YARAS [2] studied, using DNS, the transition in a separated boundary layer at two freestream turbulence levels: $Tu = 0.1\%$ and $Tu = 1.45\%$. In the low turbulence environment ($Tu = 0.1\%$), the transition was initiated by the Kelvin–Helmholtz (KH) instability mechanism. Two instability modes were reported, the first developed in the outer part of the separated shear layer and the second in the reverse-flow region near to the plate. In the higher turbulence case ($Tu = 1.45\%$), the shear layer roll-up did not appear due to the influence of streamwise-oriented streaks. BALZEN and FASEL [3] performed DNS of transition in the separated boundary layer for flow developing along the flat plate assuming various freestream turbulence levels ($Tu$ = 0–2.5%). A strong amplification of flow disturbances was noticed downstream of laminar boundary layer separation in zero-pressure gradient flow. At the higher turbulence level ($Tu = 2.5\%$) and the adverse-pressure gradient, an increased growth of the spanwise averaged Reynolds stress was observed in the separated flow region. WANG *et al.* [4] studied the breakdown of roll-up eddies on the suction side of compressor blades at the high subsonic Mach number ($Ma = 0.67$) using the LES method. The flow details were analysed at two Reynolds numbers ($Re$ = 80 000–150 000) and the zero freestream turbulence level. In all cases examined the transition process was dominated by the KH instability. SIMONI *et al.* [5] investigated experimentally the growth of disturbances in the separated flow region at various Reynolds numbers ($Re$ = 40 000–90 000) and various turbulence levels ($Tu$ = 0.65–2.87%). In low freestream turbulence cases a linear growth of streamwise fluctuations, being the effect of the KH rolls, was observed upstream of the maximum bubble displacement point. Further downstream more intense velocity fluctuations were produced. Increasing the freestream turbulence level, a change in the amplification rates of both streamwise and wall-normal fluctuations was reported. ISTVAN and YARUSEVYCH [6] measured the separated boundary layer characteristics for the flow over NACA0018 aerofoil at 4° incidence, at two chord-based Reynolds numbers ($Re = 80\,000$ and $Re = 125\,000$), and various freestream turbulence levels ($Tu = 0.06$–$1.99\%$). In all cases examined, the roll-up eddies were reported. At the lowest turbulence level ($Tu = 0.06\%$) the spanwise-oriented structures were subject to flow perturbations leading to the earlier vortex breakdown. At the increased turbulence level ($Tu = 0.51$–$1.99\%$), the stronger undulations of the spanwise-oriented vortex structures were observed owing to the formation of streaks upstream of the separation point, resulting in a highly three-dimensional breakdown of the separated boundary layer. SERNA and LAZARO [7] investigated the separated boundary layer developing over a flat plate in a divergent channel at a low freestream turbulence level ($Tu < 0.1\%$) using the hot-wire and PIV techniques. They reported a vortex shedding process originated in Kelvin–Helmholtz instability waves, which evolved into the formation of vortex blobs that later promoted the flow reattachment. They confirmed that the vortex blob suffers large deformations promoted by the strong pressure gradients at the reattachment region. ANAND and GANESH [8] studied experimentally the effect of various pressure gradient on separated boundary layer characteristics at the leading edge of an aerofoil operating at the low Reynolds number ($Re = 25\,000$). They demonstrated a strong dependence of the flow unsteadiness in the separated boundary layer on the freestream turbulence level. The transition in the separated boundary layer is mainly influenced by the Reynolds number and the freestream turbulence level. The influence of the momentum thickness Reynolds number on transition onset was accounted for in the correlations by MAYLE [9]. DELLACASAGRANDE *et al.* [10], developed improved correlations for transition onset and the spot production rate, taking into account also the influence of freestream turbulence level. Both the increase of the Reynolds number and the freestream turbulence level result in a notable reduction of the size of separation bubble.

The effect of external acoustic forcing onto the separated boundary layer development on NACA0018 aerofoil at $Re = 125\,000$ and $Tu = 0.1\%$ was experimentally studied by KURELEK *et al.* [11] and KURELEK *et al.* [12]. In the case, without acoustic excitation, a growth of disturbances was observed within the separated flow region with maximum values concentrated at the wall-normal distance corresponding to the displacement thickness. Both tonal and broadband excitation led to earlier shear layer roll-up. A reduction of the size of the separation bubble and shifting the reattachment point upstream was observed with the acoustic excitation applied. The shear layer disturbances reached higher amplitudes at earlier streamwise distances compared to the unperturbed case. The separated boundary layer was susceptible to the development of disturbances in a wide range of frequencies. The nonlinear mechanism was very likely responsible for the amplification of perturbations prior to the turbulent breakdown. Interestingly, in KURELEK *et al.* [12] the influence of standing waves on development of flow disturbances in a separated boundary layer was reported. An influence of acoustic pressure waves, generated at the trailing edge of NACA0012 profile at 2°

incidence, on the separated boundary layer, was investigated by Pröbsting and Yarusevych [13], assuming various Reynolds numbers ($Re = 65\,000$–$450\,000$). Propagation of acoustic waves resulted in formation of an acoustic feedback loop between the separation bubble and the tonal emissions at the trailing edge. The enhancement of flow disturbances with increasing the Reynolds number was reported. The amplification of disturbances was accompanied by the reduced size of the bubble on suction and pressure sides of the aerofoil.

Application of transitional RANS and hybrid RANS-LES techniques is challenging for the prediction of flows over NACA0018 aerofoil, as demonstrated by Michna and Rogowski [14] and Tangermann and Klein [15] among others. Tangermann and Klein [15] showed a strong sensitivity of the numerical results to the freestream turbulence level and turbulent length scales. Wahidi and Olçmen [16] reported differences between the measured and predicted by the $k$-$k_l$-$\omega$ model size of the separated boundary layer on the suction side of LA2573A aerofoil. It means that the separated flow physics is challenging for RANS-based transition models.

A baseline algebraic intermittency model [17, 18], which is a subject of the present study, was tested and modified by other research teams. Nering and Rup [19, 20] extended the algebraic model for the analysis of transitional flows in pipes and channels. Holman and Fürst [21, 22] coupled the algebraic model with the explicit algebraic Reynolds stress model (EARSM). The EARSM-based transition model was successfully employed for the simulation of separation-induced transition over aerofoils and for the prediction of transonic flows through VKI cascade [21, 22]. The predictive qualities of the modified algebraic model were also tested for the prediction of separated boundary layers by Louda *et al.* [23]. In the present work, attempts have been made to extend the predictive capabilities of the algebraic model widely described in [17, 18], by including the effect of external acoustic forcing on transition in a separated boundary layer. The impact of this interaction was built on the basis of an in-depth experimental study in a diffuser channel. It is expected that the extended algebraic model will be able to capture this effect with satisfactory accuracy.

## 2. Extension of algebraic model

The transport equations for the turbulent kinetic energy, $k$, and specific dissipation rate, $\omega$, have the same form as in the previous work [18, 24]:

$$\frac{Dk}{Dt} = \gamma P_k + P_{\mathrm{KH}} + P_{ac} - \beta^* k\omega + \frac{\partial}{\partial x_j}\left[\left(\nu + \sigma^* \frac{k}{\omega}\right)\frac{\partial k}{\partial x_j}\right], \tag{2.1}$$

$$\frac{D\omega}{Dt} = \alpha \frac{\omega}{k} P_k - \beta\omega^2 + \frac{\partial}{\partial x_j}\left[\left(\nu + \sigma \frac{k}{\omega}\right)\frac{\partial \omega}{\partial x_j}\right] + \frac{\sigma_d}{\omega}\max\left[\frac{\partial k}{\partial x_j}\frac{\partial \omega}{\partial x_j}, 0\right]. \tag{2.2}$$

The term $\gamma$ (see later Eq. (2.7)) is a multiplier of the production term in the $k$-equation. It is called the intermittency factor. The production term itself is defined as $P_k = \nu_s S^2$, with $\nu_s$ the small-scale eddy viscosity (defined later) and $S = \sqrt{2S_{ij}S_{ij}}$ the magnitude of the strain rate tensor. The components of the strain rate tensor are $S_{ij} = \frac{1}{2}(\partial U_i/\partial x_j + \partial U_j/\partial x_i)$. The changes for transition prediction with respect to the model equations used for a fully turbulent flow [24], are the multiplication of the production term in the $k$-equation with the intermittency factor $\gamma$ and the replacement of the turbulent viscosity by its small-scale part $\nu_s$ in the production terms of both equations. The $P_{\mathrm{KH}}$-term in Eq. (2.1) accounts for transition in the separated boundary layer caused by the Kelvin–Helmholtz instability mechanism. With respect to the previous model [18], the term $P_{ac}$ in the $k$-equation, which expresses the effect of acoustic waves on transition in a separated layer, has been introduced. The coefficients of the underlying $k$-$\omega$ model $(\alpha, \beta^*, \beta, \sigma, \sigma^*, \sigma_d)$ are according to WILCOX [24].

For modelling bypass transition in an attached boundary layer, the turbulent kinetic energy, $k$, is split into a small-scale part, $k_s$, and a large-scale part, $k_\ell$ [17, 18, 25]:

$$k_s = f_{ss}k, \qquad k_\ell = (1 - f_{ss})k. \tag{2.3}$$

The shear-sheltering effect is expressed with the $f_{ss}$ function, which employs three constants, $C_s$, $C_\chi$ and $C_k$ (Table 1). The $f_{ss}$ function is given by:

$$f_{ss} = \exp\left(-\left(\frac{C_{ss}\nu}{\sqrt{k}y}\right)^2\right), \qquad \text{with } C_{ss} = C_s(1 + f_k\chi). \tag{2.4}$$

We refer to [18] for a discussion of $f_k$ and $\chi$ functions in Eq. (2.4). The eddy viscosity of the small scales is

$$\nu_s = \frac{k_s}{\tilde{\omega}_s}, \tag{2.5}$$

with $\tilde{\omega}_s$ a limited value of $\omega$: $\tilde{\omega}_s = \max[\omega, C_{\lim}S/a_s]$, where $C_{\lim} = 7/8$, $a_s = 0.3$ [24]. The eddy viscosity of the large scales is

$$\nu_\ell = \frac{k_\ell}{\tilde{\omega}_\ell}, \tag{2.6}$$

with $\tilde{\omega}_\ell$ a limited value of $\omega$: $\tilde{\omega}_\ell = \max[\omega, C_{\lim}S/a_\ell]$ where $a_\ell = 0.6$. The effective eddy viscosity, used in the Navier–Stokes equations, is $\nu_t = \nu_s + \nu_\ell$.

The turbulence breakdown is modelled by the intermittency function defined by:

$$\gamma = \min\left(\max\left(\frac{\sqrt{k}y}{A_\gamma\nu} - 1, 0\right), 1\right), \tag{2.7}$$

where $A_\gamma$ is the constant (see Table 1). The upper half of the Table 1 summarises the model constants that are relevant for bypass transition. The constants $A_\gamma$, $C_s$,

TABLE 1. Transition model constants.

<table>
<tr><td colspan="9">Bypass transition</td></tr>
<tr><td>$A_\gamma$</td><td colspan="2">$C_s$</td><td>$C_\chi$</td><td colspan="2">$C_k$</td><td>$a_s$</td><td colspan="2">$a_\ell$</td></tr>
<tr><td>12.0</td><td colspan="2">21.0</td><td>10.0</td><td colspan="2">6.0</td><td>0.30</td><td colspan="2">0.6</td></tr>
<tr><td colspan="9">Separation-induced transition & acoustic forcing</td></tr>
<tr><td>$C_{\mathrm{KH}}$</td><td>$A_{\mathrm{KH}}$</td><td>$C_{\mathrm{Kleb}}$</td><td>$a_\omega$</td><td>$b_\omega$</td><td>$a_\gamma$</td><td>$b_\gamma$</td><td>$c_w$</td><td>$C_{ac}$</td></tr>
<tr><td>2</td><td>550</td><td>0.155</td><td>200</td><td>5</td><td>0.95</td><td>150</td><td>2</td><td>0.1</td></tr>
</table>

$C_\chi$, $C_k$ and $a_s$ are the same as in the previous model version [18]. The constant $a_\ell$ has been changed from 0.45 to 0.60, to better reproduce the transitional boundary layer characteristics approaching the turbulent flow [26].

The $P_{\mathrm{KH}}$-term in the turbulent kinetic energy transport equation (Eq. (2.1)) accounts for the breakdown of the separated shear layer in the low-freestream turbulence environment. In the separated laminar boundary layer, both the shear-sheltering term (Eq. (2.4)) and the intermittency function (Eq. (2.7)) attain very low values. The standard production terms ($P_k$) are thus very low. By activation of the supplementary boosting function ($P_{\mathrm{KH}}$) the turbulent kinetic energy is enlarged. With sufficiently high values of $k$, the intermittency function (Eq. (2.7)) becomes active. The $P_{\mathrm{KH}}$-term (KH) is the same as in the previous model version [18]:

$$P_{\mathrm{KH}} = C_{\mathrm{KH}}(1-\gamma)F_{\mathrm{KH}}\nu S^2, \tag{2.8}$$

with

$$F_{\mathrm{KH}} = \min\left(\max\left(\frac{R_S}{2.2A_{\mathrm{KH}}} - 1, 0\right), 1\right) \quad \text{and} \quad R_S = \frac{S\,y^2}{\nu}. \tag{2.9}$$

The $P_{\mathrm{KH}}$-term is a simplified form of boosting term in the local correlation-based intermittency transport model (LCTM) by MENTER *et al.* [27]. It becomes active when the $R_s$ function reaches a critical value, equal to 2.2 $A_{\mathrm{KH}}$.

A new $P_{ac}$ term in a transport equation of turbulent kinetic energy (Eq. (2.1)) is introduced to mimic the effect of external acoustic forcing on enhancement of flow disturbances inside the separated boundary layer:

$$P_{ac} = C_{ac} f_{ac} \nu S^2, \tag{2.10}$$

where $C_{ac}$ is the model constant (Table 1). We show the tuning of the $C_{ac}$ constant in next Section 3. The $f_{ac}$ function is a sensor for detection of the front part of a separated boundary layer. It is defined as the product of three functions:

$$f_{ac} = f_\gamma f_\omega f_w, \tag{2.11}$$

where

$$f_\gamma = \frac{1}{1+\exp[b_\gamma(\gamma - a_\gamma)]}, \qquad f_\omega = \frac{1}{1+\exp[-b_\omega(Re_\omega - a_\omega)]}, \tag{2.12}$$

$$f_w = \exp\left(-\left(\frac{Re_t}{c_w}\right)^2\right), \qquad \text{with } Re_\omega = \omega y^2/\nu \text{ and } Re_t = k/(\omega\nu). \tag{2.13}$$

The $f_\gamma$, $f_\omega$ and $f_w$ functions are the same as used in previous work [26]. The first two functions were also employed in [28]. In [26] the $f_\gamma$, $f_\omega$ and $f_w$ functions were used for detection of the front part of the separated boundary layer with purpose to model the effect of the Klebanoff disturbances, perturbing the Kelvin–Helmholtz rolls, onto the transition process. In this work, the $f_\gamma$, $f_\omega$ and $f_w$ functions are employed with the aim to model the enhanced mixing caused by the external acoustic forcing.

The supplementary production term (Eq. (2.10)) is defined in a similar way as the Kelvin–Helmholtz-instability term (Eq. (2.8)), so with the product of molecular viscosity and the magnitude of the strain-rate tensor squared. Kurelek *et al.* [11] observed an earlier shear layer roll-up, under both tonal and broadband acoustic forcing, resulting in an increased turbulent shear stress (see their Fig. 6). The observation from [11] suggests a similar way of modelling of the effect of acoustic waves, as with the Kelvin–Helmholtz-instability term. Thus the influence of acoustic forcing is taken into account by the supplementary production term, $P_{ac}$ (Eq. (2.10)) added to the $k$-equation (Eq. (2.1)). The sensitivity to *SPL* was also reported in [11]. But the present transition term (Eq. (2.10)) is not designed to take into account the effect of varying *SPL*. As we show later, the model component is calibrated to take into account the maximal effect of acoustic waves on the separated-flow transition, which was observed in the reference experiments. This effect seems to be most important from the point of view of the design of aircraft elements. The effect of varying *SPL* might be later incorporated into the current modelling framework when more experimental/DNS data will be available.

## 3. Calibration of the model term for separation-induced transition influenced by acoustic waves

The key parameter in Eq. (2.10) is the model constant, $C_{ac}$. Selection of this constant has been performed based on experimental data obtained at Częstochowa University of Technology (CUT), Poland [29]. The test case consists of a flat plate inclined at 1° with respect to a horizontal line. Figure 1 shows the schematic of 2D domain together with coordinate system, types of boundary conditions and locations of measuring traverses. The upper wall was shaped to

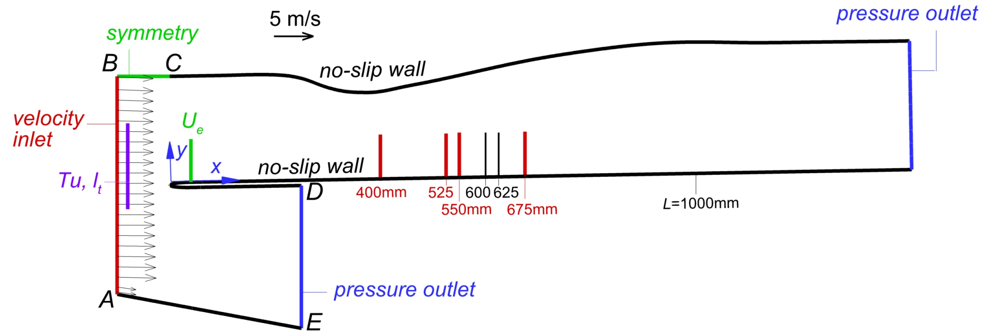

FIG. 1. Schematic of the computational geometry for simulation of the flow along the flat plate, coordinate system, types of the boundary conditions and vertical lines showing the location of measuring traverses. The plate is inclined at 1° with respect to horizontal line.

impose a desired pressure gradient typical for the suction side of the blade of axial compressor, where a strong adverse pressure gradient (APG) is present in the second part of the channel. The coordinates of test section are provided in Appendix A. A throat is placed at streamwise distance $x = 381\,\text{mm}$ ($x/L = 0.381$) from the plate leading edge ($L = 1000\,\text{mm}$ is the nominal length of the plate). The distance between the plate surface and upper wall at the throat is $y = 165\,\text{mm}$ ($y/L = 0.165$). The laminar boundary layer develops along a flat plate and separates at $x/L = 0.525$. The transition to turbulence occurs in the separated boundary layer. The Reynolds number ($Re_{L,s}$) based on the streamwise distance between the plate leading edge and boundary layer separation point and mean velocity at the boundary layer edge at reference plane $x = 40\,\text{mm}$ ($x/L = 0.04$) is equal to 174 000. The freestream turbulence level, measured at distance $x = -80\,\text{mm}$ ($x/L = -0.08$), is equal to $Tu = 0.6\%$ (Fig. 1). The velocity measurements were performed at selected streamwise distances with the use of a single hot-wire probe. The selected traverses are shown by vertical lines in Fig. 1, denoted by $x = 400$, 525, 550, 600, 625 and 675 mm. Here we report the results at $x = 400$, 525, 550 and 675 mm (shown by red colour). For the excited case, the flow was exposed to the pink noise characterized by the sound pressure level equal to 135 dB in the frequency range between 100 and 650 Hz. The acoustic excitation field contained acoustic reflections as the wind tunnel consists of all rigid walls and no acoustic treatments were applied. However, during the experimental tests, the acoustic excitation field was measured at 18 points, non-uniformly distributed inside the wind tunnel test section. The maximum $SPL$ difference was at the level of approximately 4 dB in the 1/3 octave band. This confirms that no strong standing waves were present inside the test section during the experiments.

The simulations were performed on 2D grid consists of 161 000 cells. The near-wall regions were discretised with the structured mesh consists of 20–30 cells in wall-normal direction (boundary layer thickness). The unstructured mesh, consisting of quadrilateral cells, was employed outside of the boundary layers. The maximal value of $y^+$ was less than 0.6 along the flat plate and less than 2 along other walls. The grid was sufficiently fine to ensure grid-independence of the results (see Appendix B for a grid-sensitivity study). The fluid was assumed as incompressible. The coupled pressure-based solver was used for solution of governing equations. The second-order upwind scheme was employed for discretization of convective terms in momentum and turbulence model equations. The turbulence model was implemented in the ANSYS Fluent finite volume code through the User Defined Function (UDF) – functionality. The normalized residuals were driven to $10^{-6}$ level for solution of governing and transport equations.

The inlet values of mean $x$- and $y$-velocity components and root-mean-square (r.m.s.) of fluctuating velocities were imposed in simulation according to measurements [29]. The data were provided along lines denoted by $AB$ and $DE$ in Fig. 1, using the $x$-wire probe. The prescription of the inlet values of the turbulent kinetic energy, $k = \frac{1}{2}(\overline{u'u'} + \overline{v'v'} + \overline{w'w'})$, required estimation of the Reynolds normal stress component $\overline{w'w'}$, because only the $\overline{u'u'}$ and $\overline{v'v'}$ components were available from the 2D hot-wire measurements. In current work, the $\overline{w'w'}$ component was estimated by $\overline{w'w'} = \overline{v'v'}$ along $AB$ line. The definition of the inlet profile of the specific dissipation rate, $\omega = \sqrt{k}/(\beta^* \ell_t)$, required estimation of the integral length scale, $l_t$. The $l_t$-values were measured in few points along vertical line denoted by '$Tu$, $l_t$' symbol in Fig. 1 and averaged. The mean value was equal to $l_t = 100\,\mathrm{mm}$. The inlet profiles of mean $x$-, $y$-velocity components, $k$ and $\omega$ along $AB$ line were smoothed by fitting a low-order polynomial, for use in numerical simulations. At the outlet of the computational domain, above the plate, a constant value of the static pressure was imposed, according to measurements. The static pressure profile was adjusted at the second domain outlet ($DE$ line in Fig. 1), to match the measured mean velocity profile there. In measurements, the construction elements were placed downstream of $DE$ line, so adjustment of flow conditions was needed to reproduce the losses there. Figure 2a compares the measured and predicted mean $x$-velocity along $DE$ line in Fig. 1. Figure 2b shows a comparison between measured and predicted, by the algebraic intermittency model, the static pressure profile at 100 mm above the plate surface. The apparent consistency of results confirms correctness of specification of the boundary conditions for the mean flow variables along $AB$-inlet and at both outlets.

For a proper calibration of the acoustic model term, a good correspondence between measured and predicted freestream turbulence levels, for a natural flow (without acoustic excitation), has to be assured first. For this purpose, the evo-

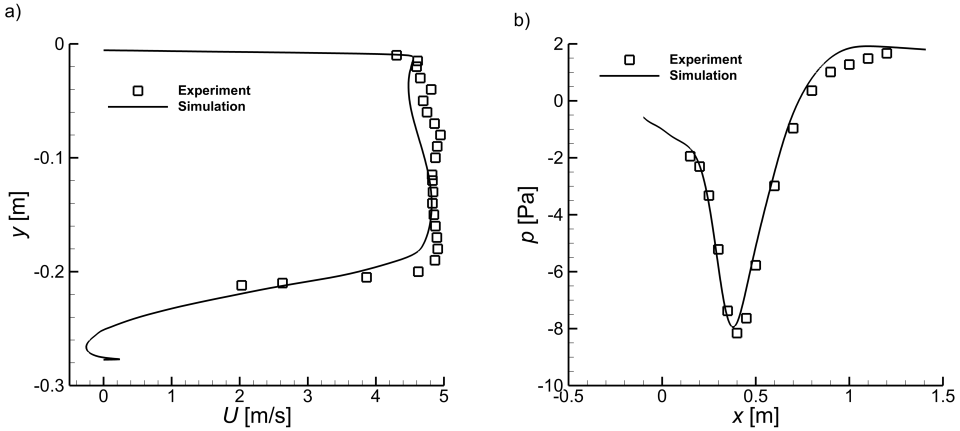

Fig. 2. Flow along a flat plate ($Re_{L,s} = 174\,000$, $Tu = 0.6\%$). Predicted and measured a) mean streamwise velocity at outlet from the computational domain below the plate (see $DE$ line segment in Fig. 1) and b) pressure distribution at 100 mm above the plate surface.

lutions of the mean velocity and r.m.s. of fluctuating velocity profiles are presented in Fig. 3 at four streamwise distances: $x = 400$ mm (laminar flow), 525 mm (separation point), 550 mm (separated boundary layer) and 675 mm (turbulent boundary layer recovery) for an unexcited flow. The modelled fluctuating velocity is computed from the turbulent kinetic energy, assuming isotropy. The mean velocity profiles are in good agreement with measurements inside the boundary layer. Small difference is visible in the freestream, were the predicted mean velocity profiles at distances $x = 400$, 525 and 550 mm are about 3–4% lower than the measured ones. This difference might be due to ambiguity in the prescription of the mean and turbulence flow variables near to the upper contoured wall. Note that the tripping element was imposed in measurement in front part of the upper wall (downstream the point $C$ in Fig. 1) to avoid separation of the boundary layer there. The presence of a tripping element was not accounted for in the present study, but the flow was assumed as fully-turbulent near to the upper wall. This was achieved by defining the shear-sheltering (2.3) and intermittency (2.7) terms equal to unity above the wall-normal distance $y = 150$ mm. There is also small difference between predicted and measured velocity close to wall in the separated boundary layer at $x = 550$ mm (Fig. 3c). As demonstrated in later Fig. 4, this is due to somewhat too abrupt transition reproduced with the present model. Good agreement is reported between measured and predicted freestream values of fluctuating velocity components at all streamwise distances in Fig. 3. This confirms quality of the inlet conditions along $AB$ line (Fig. 1). One can see differences between predicted and measured fluctuating velocity components close to the wall (Fig. 3a, b and c). The measured peak values of fluctuating

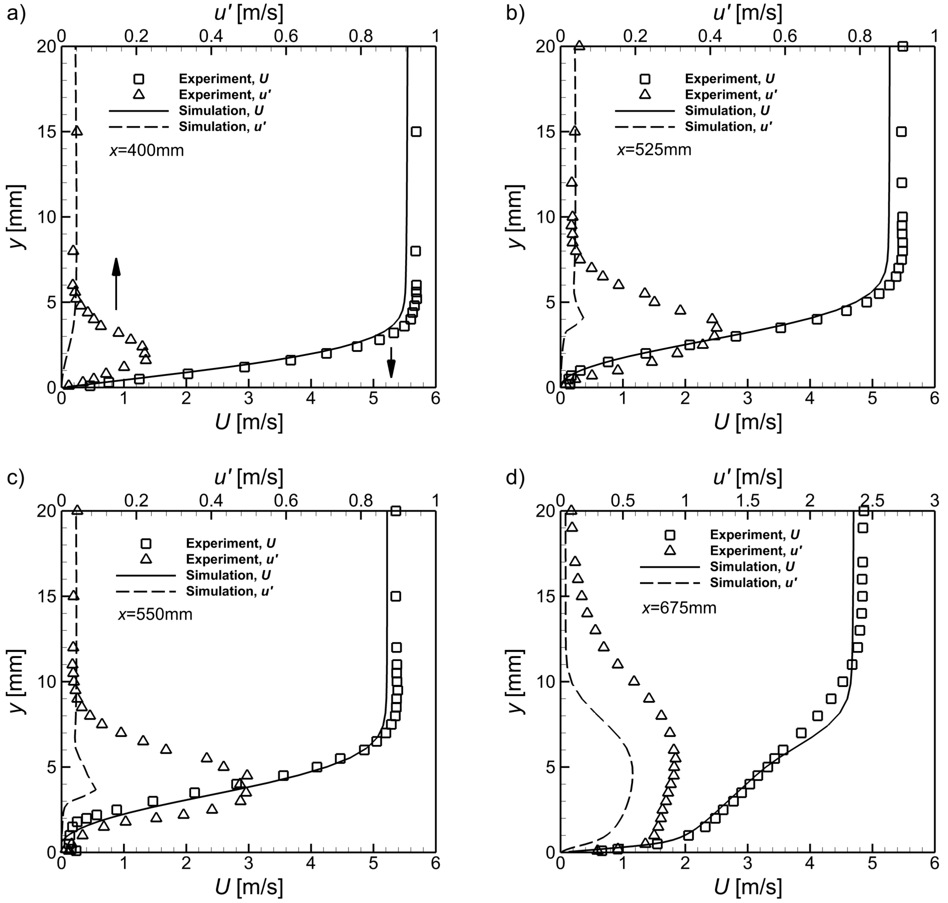

Fig. 3. Flow along a flat plate with adverse pressure gradient ($Re_{L,s} = 174\,000$, $Tu = 0.6\%$). Predicted and measured profiles of mean streamwise velocity, $U_x$, and r.m.s. of fluctuating velocity components, $u'$, for a natural flow (without acoustic excitation) at streamwise distances: a) $x = 400$ mm (laminar flow), b) 525 mm (separation), c) 550 mm (separated boundary layer), and d) 675 mm (turbulent boundary layer recovery) from the plate leading edge.

velocity components at streamwise distances 400, 525 and 550 mm are due to the Klebanoff streaks. A discussion on this subject, confirming the existence of the Klebanoff modes is given in Section 4. Note that the current algebraic intermittency model is not meant to model the evolution of the large-scale Klebanoff disturbances (streaks) in the pseudo-laminar boundary layer. The model has been constructed to account for the penetration of small-scale turbulence, towards the wall, using the shear-sheltering term (Eq. (2.3)). This effect is well reproduced in the present model. Figure 3d shows the mean and fluctuating flow details in the turbulent boundary layer flow. Although the mean velocity profile is well predicted, the fluctuating velocity component is underestimated. The power spectra at the streamwise distances $x = 625$ and 650 mm (see later Fig. 7a) show accumulation of energy in the frequency range ($f = 20$–80 Hz). This energy results from vortex shedding in the separated boundary layer. The unsteady flow character associated with vortex shedding cannot be fully reproduced in the present steady RANS simulation. Note that similar quality results were obtained by ZHOU *et al.* [30] for simulation of the flow over A-Aerofoil using the $\gamma - \bar{R}e_{\theta t}$ and hybrid DDES/$\gamma - \bar{R}e_{\theta t}$ models. So one can conclude that a good agreement is achieved between measured and predicted mean and fluctuating flow details along the plate (Fig. 3).

With the model validated for a natural flow (without acoustic excitation), the next step was to include the effect of acoustic forcing. First, a role of the baseline $P_{\mathrm{KH}}$ production term is discussed in Fig. 4a for simulation of the CUT flat plate without the acoustic excitation. The two simulation results are presented, one obtained with the present model (denoted by without acoustic forces) and one with inactive the $P_{\mathrm{KH}}$ production term in Eq. (2.1) (denoted by without acoustic forces, inactive $P_{\mathrm{KH}}$-term). The first result shows quite good agreement with an experiment (see discussion later on too low peak value of $H_{12}$). The second result (inactive $P_{\mathrm{KH}}$-term) shows significantly delayed transition onset, resulting in a too high peak value of a shape factor along the plate at $x = 0.65$ m. Clearly, the role of $P_{\mathrm{KH}}$-term is essential for proper accounting for the separation-induced transition. Figure 4b shows measured and predicted by the algebraic model shape factors along the flat plate in cases without and with the acoustic excitation with the *SPL* of 135 dB [29]. In the experiment, the background noise for the unexcited

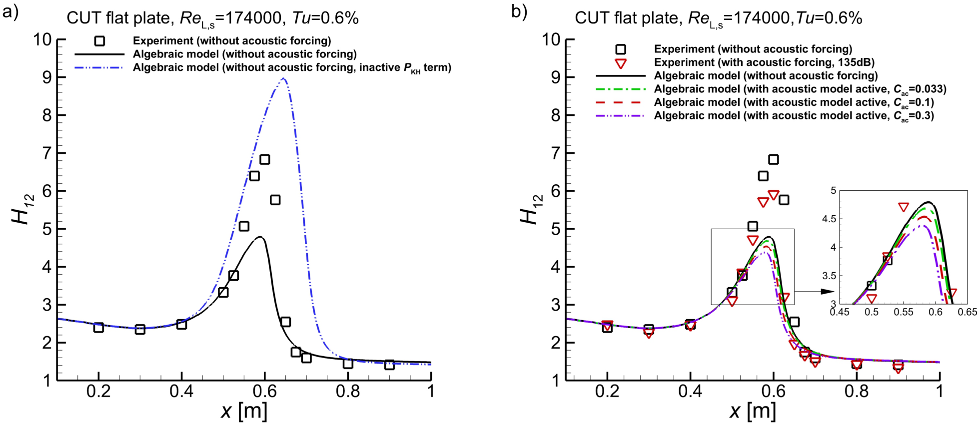

FIG. 4. Flat plate with an adverse pressure gradient at $Re_{L,s} = 174\,000$, $Tu = 0.6\%$. Distribution of the shape factor along the plate without and with the acoustic excitation.

case was equal to 89 dB. The difference in the *SPL* level is thus 46 dB. The numerical results were obtained with the three values of $C_{ac}$ coefficient equal to 0.033, 0.1 and 0.3. The peak values of $H_{12}$ are underestimated in simulations (Fig. 4b). This is due to modelling of the KH instability by production of turbulent kinetic energy in the instability zone of a separated layer [18, 26]. The reduction in the transition onset Reynolds number, $Re_{x,s-t}$, in the case with the acoustic excitation is well reproduced by the model using $C_{ac} = 0.1$. More detailed insight on transitional flow characteristics is provided in Table 2. The table summarizes the measured and predicted locations of boundary layer separation, the momentum thickness Reynolds number at separation, $Re_{\theta,s} = \theta_s \cdot U_{e,s}/\nu$ ($\theta_s$ and $U_{e,s}$ are the momentum thickness and edge velocity at separation), and the transition onset Reynolds number, $Re_{x,s-t} = \Delta x_{s-t} U_{e,s}/\nu$ ($\Delta x_{s-t}$ is the distance between the separation and transition onset points), in unexcited and exited cases. It should be noted that in the experiment, the separation onset was difficult to detect using the single hot-wire technique due insensitivity of the sensor element to the flow direction. Therefore, the detachment point was determined by an indirect method using the calculated values of the shape factor parameter, which, as an integral measure, is less sensitive to measurement errors near to the wall. A relationship for the laminar boundary layer, proposed by Drela and Giles [31], was used for this purpose. A correctness of separation point determination was approved by means of a smoke visualization technique. In simulation, the separation location was determined based on wall shear stress, $\tau_w$, profile (point

Table 2. Measured and predicted values of boundary layer separation point, $(x/L)_s$, momentum thickness Reynolds number at separation, $Re_{\theta,s}$, and transition onset Reynolds number, $Re_{x,s-t}$, for the CUT flat plate at $Re_{L,s} = 174\,000$, $Tu = 0.6\%$. The numerical data are obtained for different values of $C_{ac}$ constant in Eq. (2.10). The relative error in % is given in the brackets.

| Acoustic excitation | $C_{ac}$ | $(x/L)_s$ Experiment | $(x/L)_s$ Simulation | $Re_{\theta,s}$ Experiment | $Re_{\theta,s}$ Simulation | $Re_{x,s-t}$ Experiment | $Re_{x,s-t}$ Simulation |
|---|---|---|---|---|---|---|---|
| Excitation inactive | – | 0.525 | 0.520 (1%) | 293 | 300 (2.4%) | 27145 | 26492 (2.4%) |
| Excitation active (135 dB) | 0.033 | 0.525 | 0.525 (0%) | 280 | 300 (7.1%) | 23287 | 24804 (6.5%) |
| Excitation active (135 dB) | 0.100 | 0.525 | 0.525 (0%) | 280 | 300 (7.1%) | 23287 | 23366 (0.3%) |
| Excitation active (135 dB) | 0.300 | 0.525 | 0.525 (0%) | 280 | 300 (7.1%) | 23287 | 21569 (7.4%) |

at which $\tau_w$ changes sign from positive to negative). The transition onset point ($Re_{x,s-t}$ formula) was determined both in the measurement and simulation at the streamwise distance, at which the maximal value of displacement thickness was observed along the plate [6]. In the unexcited case (Table 2) a relative error between measurements and simulation is less than 2.5%. It shows credibility of the numerical results. In the case with acoustic excitation, the lowest relative error (0.3%) between the measured and predicted value of the transition onset Reynolds number, $Re_{x,s-t}$, was obtained with $C_{ac} = 0.1$. Larger error levels (6–7%) were reported with $C_{ac} = 0.033$ and 0.3. Thus the $C_{ac} = 0.1$ is selected for the further study.

Note that the effects due to acoustic reflections at the wind tunnel walls are included in the present mathematical modelling ($C_{ac}$ constant), since the model was calibrated based on the experimental data obtained for the acoustic excitation with inherent acoustic reflections. It was the intention of the experimental tests to include the acoustic reflections which are typical for aerospace and turbomachinery applications.

## 4. Functioning of the transition model under acoustic forcing

In this section, illustration of functioning of the algebraic intermittency model is provided in the cases without and with the acoustic excitation. Figure 5 shows the contour plots of mean streamwise velocity, $P_{\mathrm{KH}}$-term (Eq. (2.8)), intermittency factor $\gamma$ (Eq. (2.7)) and the turbulent kinetic energy, $k$, in an unexcited case. The separated boundary layer region is visible in Fig. 5a. The clipped zone corresponds to the negative values of streamwise velocity. The $P_{\mathrm{KH}}$ production term is active in the front part of the separated boundary layer (see panels (a) and (b)). As mentioned, this term is responsible for modelling of shear layer breakdown due to the Kelvin–Helmholtz instability [18]. The activity of $P_{\mathrm{KH}}$-term in panels (a) and (b) can be better understood by verifying the measured power spectra density of streamwise velocity fluctuating presented in Fig. 7a. The spectra show amplification of the KH-instability at central frequency $f = 48\,\mathrm{Hz}$ (see also Sokolenko *et al.* [29]) at streamwise distances 400, 525 and 550 mm from the plate leading edge. This instability is modelled in the present model by the $P_{\mathrm{KH}}$ production term shown in Fig. 5a and b. Strong amplification of fluctuations is visible in Fig. 7a at the streamwise distance $x = 600\,\mathrm{mm}$ in the band of frequencies centred on $f = 48\,\mathrm{Hz}$. Further downstream ($x = 625$ and 650 mm) the energy content of velocity fluctuations becomes rapidly distributed over a much wider range of frequencies. This process, resulting from the breakdown process of the roll-up eddies, is taken into account in the present model by a local increase of the turbulent kinetic energy as a consequence of the boosting effect of the $P_{\mathrm{KH}}$-production term in the $k$-equation. It activates the intermit-

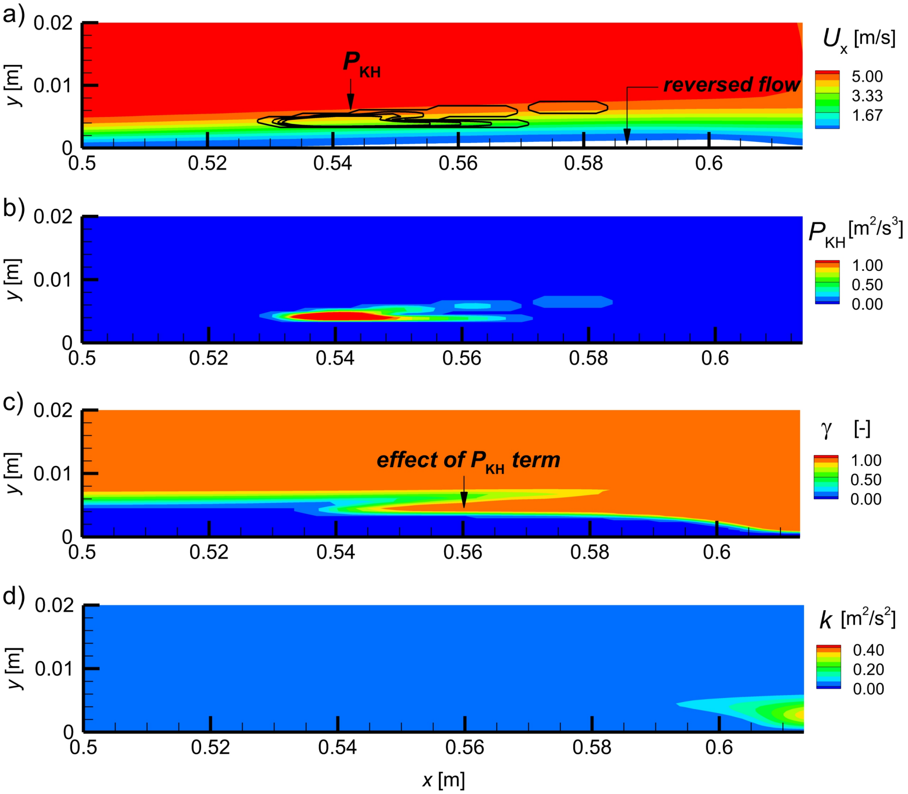

Fig. 5. Flow along a flat plate without the acoustic excitation. The contour plots of a) streamwise velocity, $U_x$, b) $P_{\mathrm{KH}}$ production term, c) intermittency factor $\gamma$ and d) the turbulent kinetic energy, $k$. The contour plot of $P_{\mathrm{KH}}$ is reproduced on a panel (mean velocity), by means of contour lines, for purpose of comparison with results in Fig. 6.

tency term in the middle part of the boundary layer (Fig. 5c) and causes the transition to turbulence. The result is the reduction of the size of the separation bubble, as discussed in earlier Fig. 4a.

Figure 6 shows the contour plots of a) mean streamwise velocity superimposed with contour lines of the $P_{\mathrm{KH}}$ production term (Eq. (2.8)), b) the $P_{ac}$ production term (Eq. (2.10)), c) the intermittency factor $\gamma$ (Eq. (2.7)) and d) the turbulent kinetic energy $k$. The contour plot of $P_{ac}$-term is shown together with the measured profile of displacement thickness, $\delta^*$, denoted by a dash-dotted line (panel b). The first observation is that the activity zone of the $P_{\mathrm{KH}}$-term is now smaller than in the unexcited case discussed above (Fig. 5a). This is due to the fact that supplementary turbulence is produced in the zone determined by sum of $P_{ac}$- and $P_{\mathrm{KH}}$-terms (see Eq. (2.1)), with respect to the activity domain of a single $P_{\mathrm{KH}}$-term in unperturbed case (Fig. 5a). The second observation is

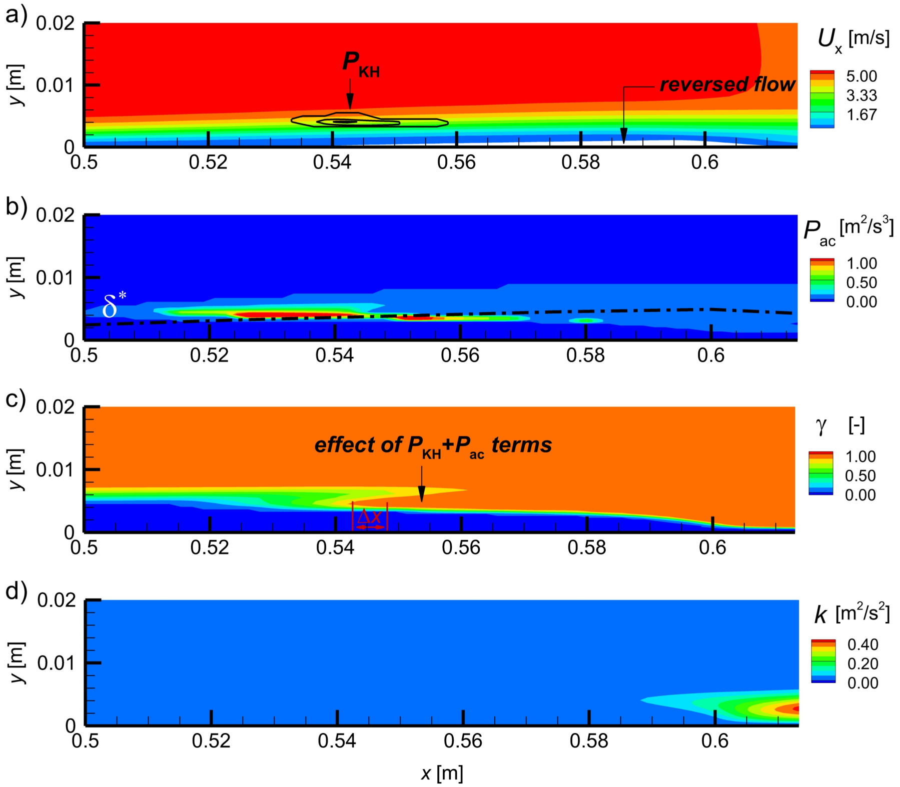

FIG. 6. Flow along the flat plate with acoustic excitation. Contour plots of a) streamwise velocity, $U_x$, together with contour lines of the $P_{\mathrm{KH}}$ term (levels 0.2, 0.4 and 0.6 $\mathrm{m}^2/\mathrm{s}^3$ are shown), b) $P_{ac}$-term, c) $\gamma$ and d) $k$. The dashed-dotted line in panel (b) shows the measured profile of the displacement thickness, $\delta^*$, along the plate. $\Delta x$ in panel c shows the difference in location of intermittency patch with respect to the unexcited case (Fig. 5c).

that the $P_{ac}$ production term is activated near to the displacement thickness line (Fig. 6b). This activity is in agreement with measurements by KURELEK *et al.* [11]. KURELEK *et al.* [11] reported an increase of turbulent shear stress inside the separated boundary layer, along $\delta^*$-line under both tonal and broadband acoustic forcing. This effect is modelled now by the supplementary $P_{ac}$-term in the $k$-equation. The boosting effect of $P_{\mathrm{KH}}$ and $P_{ac}$ production terms is also visible on contour plots of intermittency (Fig. 6c) and $k$ (Fig. 6d). It leads to a reduced size of the separation bubble (Fig. 4b) and a smaller value of the transition onset Reynolds number in the excited flow (Table 2), compared to unperturbed flow. In Fig. 6a and b a somewhat broader activity zone of $P_{ac}$ and $P_{\mathrm{KH}}$ production terms, with respect to the activity region of a single $P_{\mathrm{KH}}$ term in Fig. 5a, can be understood by analysing the measured power spectra density in Fig. 7b in flow with acoustic excitation (loudspeaker). The spectra are analysed at the same locations as in the unexcited case (Fig. 7a). One can see much broader energy content, centred now on frequency $f = 64\,\text{Hz}$, already at streamwise distances 400, 525 and 550 mm, with respect to energy content of fluctuating velocity in an unexcited case (Fig. 7a, $f = 48\,\text{Hz}$). The increased energy level is also observed for frequencies $f > 100\,\text{Hz}$. This last increase is clearly caused by acoustic excitation by the loudspeaker in the frequency range 100–650 Hz. More rapid redistribution of energy is also observed in the broader range of frequencies at the downstream distance $x = 600\,\text{mm}$ (centred on $f = 64\,\text{Hz}$). This justifies a selection of the broader activity domain of $P_{ac}$ and $P_{\text{KH}}$ production terms in the case with acoustic excitation compared to the activity zone of $P_{\text{KH}}$-term in the unexcited case.

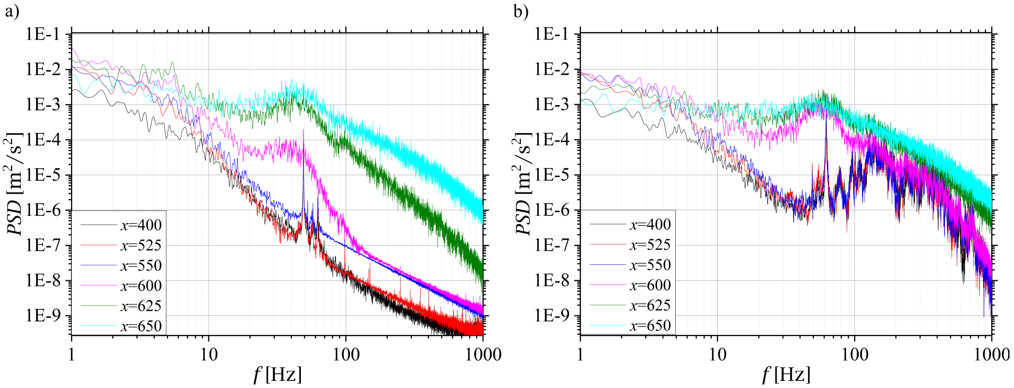

Fig. 7. Measured power spectra density ($PSD$) at streamwise distances, $x = 400$, 525, 600, 625 and 650 mm and wall-normal distance corresponding to maximal value of r.m.s. of fluctuating velocity for CUT flat plate, a) without the acoustic excitation and b) with the acoustic excitation at the $SPL$ of 135 dB. The unit of $PSD$ is $\text{W}/(\text{kg}\cdot\text{Hz}) = \text{m}^2/\text{s}^2$.

The breakdown process of the roll-up eddies, around the central frequencies $f = 48\,\text{Hz}$ and 64 Hz, was discussed with Fig. 7, in the unexcited and excited cases, respectively. As demonstrated in our previous work [29] the dominant instability Strouhal numbers ($St_\theta = f\theta_s/U_{e,s}$), computed with $f = 48\,\text{Hz}$ and 64 Hz, correspond well with data reported in the reference experiment, suggesting the Kelvin–Helmholtz instability mechanism. It seems also useful to analyse the characteristics of low-frequency events observed in Fig. 7 ($f = 1$–$10\,\text{Hz}$), since they are responsible for a significant part of energy in laminar and separated flow regions both in unexcited (Fig. 7a) and exited (Fig. 7b) cases. It can be assumed, based on the literature review [32], that these low-frequency fluctuations indicate the presence of the Klebanoff streaks in the pseudo-laminar boundary along the flat plate. To confirm this assumption, the average wavelength, $\lambda$, of the Klebanoff streaks was estimated using the correlation by Lengani *et al.* [32]

as $\lambda = 10.5\delta^*$ ($\delta^*$ displacement thickness). With the mean value of r.m.s. in Fig. 3a, b and c approximately equal to $u' = 0.1$, 0.2 and 0.25 m/s, the average frequency ($f = u'/\lambda$, Hz) of the Klebanoff streaks is estimated as: $f = 6.8$, 6.14 and 5.9 Hz. This estimation is in good agreement with energy content of low-frequency forms ($f = 1$–10 Hz) in Fig. 7. It is worth to mention that the streaks forming upstream of separation were also observed for the flow over NACA0018 aerofoil in the low and medium/high freestream turbulence environment ($Tu =$ 0.51–1.99%) in the experiments by ISTVAN and YARUSCHEVYTCH [6]. This shows that the peak values on fluctuating velocity components in Fig. 3a, b and c are due to the Klebanoff streaks.

## 5. Model validation

Validation of the proposed acoustic forcing model was performed for the flow over NACA0018 aerofoil, experimentally studied by KURELEK *et al.* [11] and KURELEK *et al.* [12]. The experiments were performed in the wind tunnel section which was 2.44 m long and had the cross-section equal to $0.61 \times 0.61\,\mathrm{m}^2$. The chord length $c$ and span of the aerofoil was equal to 0.2 and 0.61 m, respectively. The aerodynamic flow angle was equal to 4°. The Reynolds number, based on the chord length (c) and the mean velocity at inlet, was equal to $Re = 125\,000$. The freestream turbulence level was less than 0.1%. The flow was essentially 2D at the midspan owing to a large span to the chord ratio. We refer to the work [33] for discussion of flow two-dimensionality. The boundary layer on the aerofoil pressure side was tripped at $x/c = 0.4$ by three-dimensional roughness elements to limit the effect of the acoustic feedback loop mechanism.

The steady RANS simulations, with application of the algebraic intermittency model, have been performed on 2D domain of length and height equal to $1.3\,\mathrm{m} \times 0.61\,\mathrm{m}$ ($L_x \times L_y$). The aerofoil was placed at a streamwise distance equal to 0.3 m downstream of the inlet plane. The leading edge was at $x = 0$, $y = 0$. A constant value of $x$-velocity component was applied at the domain inlet to match the measured Reynolds number ($Re = 125\,000$). The inlet velocity vector was perpendicular to the inlet line (2D). The aerofoil was rotated by $\alpha = 4^\circ$ to reproduce the experimental conditions. The slip-wall conditions were superimposed on the top and bottom sides of the domain. The no-slip conditions were superimposed on the aerofoil's surface. At the outlet, the constant value of the static pressure was imposed. In measurements, the value of the freestream turbulent intensity and the longitudinal integral length scale measured at the position of the leading edge of the aerofoil, without the aerofoil present in the test section, was equal to $Tu = 0.1\%$ and $l_{int} = 0.2c = 0.04\,\mathrm{m}$, respectively. In simulation, the inlet values of turbulent intensity, $Tu$, and the dissipation length scale, $L_\varepsilon = k^{3/2}/\varepsilon$, were determined following the work by

GRAMESPACHER *et al.* [34] to match the measurements by KURELEK *et al.* [11]. The dissipation length scale was estimated as $L_\varepsilon = 60\% l_{int}$ [34]. We refer also to our previous work [26] for discussion of the inlet values of $k$ and $\omega$ for grid turbulence. Figure 8 shows the turbulent intensity, $Tu = \sqrt{2k/3}/U$ predicted by the algebraic model, (with $U$ the local mean velocity magnitude) and an integral length scale along four horizontal lines placed at $y = 0.15\,\mathrm{m}$ ($y/c = 0.75$), $0.075\,\mathrm{m}$ ($y/c = 0.375$), $-0.75\,\mathrm{m}$ ($y/c = -0.75$) and $-0.15\,\mathrm{m}$ ($y/c = -0.375$). The lines are relatively far from the aerofoil surface, but influence of the aerofoil is still visible, especially on $Tu$-profiles (Fig. 8a). At distance $x = 0$ the freestream turbulence intensity varies between 0.095 and 0.105%. The integral length scale equals to $l_{int} = 0.04\,\mathrm{m}$ there (Fig. 8b). Thus, the results prove the correctness of specification of the inlet values for the turbulence model.

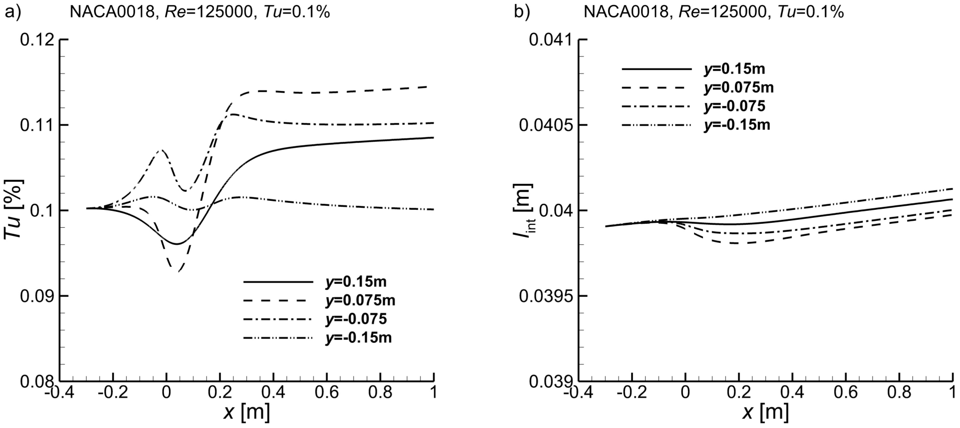

FIG. 8. Flow over NACA0018 aerofoil at $Re = 125\,000$, $Tu = 0.1\%$. Profiles of a) freestream turbulent intensity [%] and b) integral length scale [m] along horizontal lines at $y = 0.15, 0.075, -0.75$ and $-0.15\,\mathrm{m}$.

A high quality block-structured mesh was constructed with total number of cells equal to 128 000. The C-type mesh was employed around the aerofoil's surface with thickness of the near-wall zone equal to 60 mm. About 60 cells were employed in the wall-normal direction of the near-wall zone with the growth rate of elements was equal to 1.1. The maximal value of $y^+$ at the aerofoil's surface was equal to 1.4 (leading edge) while for most of the aerofoil's surface the $y^+$ values were close to 0.6.

The flow was treated as an incompressible. The pressure-based coupled solver ANSYS Fluent was used to solve the time-averaged Navier–Stokes equations. The specifications of discretisation schemes were the same as in the CUT flat plate case, discussed above. The pressure side boundary layer was tripped by putting

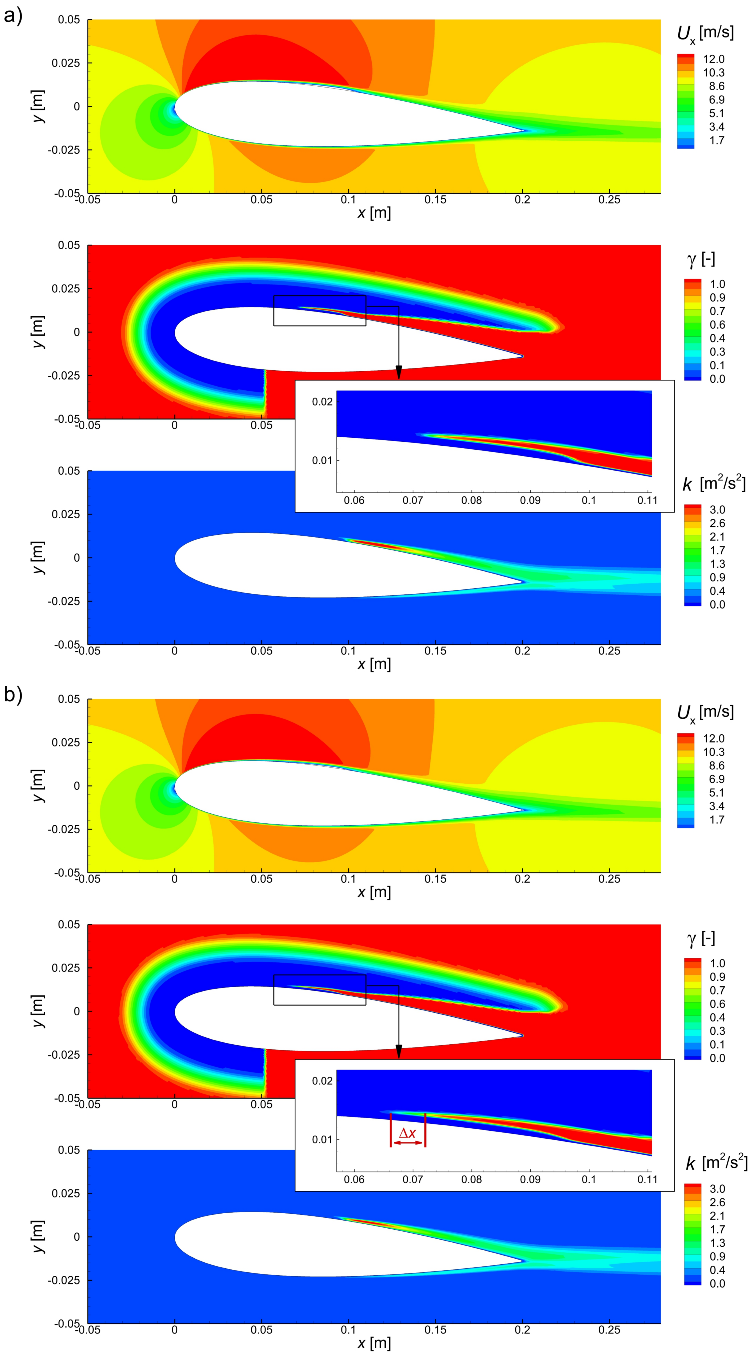

FIG. 9. Fig. 9. Flow over NACA0018 aerofoil at $Re = 125\,000$, $Tu = 0.1\%$. Contour plots of $x$-velocity component, $U_x$, intermittency factor $\gamma$ and the turbulent kinetic energy, $k$ in flows a) without and b) with active acoustic excitation term. $\Delta x$ in panel b shows the difference in location of intermittency patch with respect to unexcited case (panel a).

the intermittency factor equal to unity downstream of $x/c = 0.4$ (see Fig. 9, intermittency factor). The normalized residuals for the flow and turbulence model equation were driven below the $10^{-6}$ level.

Figure 9 shows the contour plots of mean $x$-velocity, intermittency factor $\gamma$ and turbulent kinetic energy, $k$, for simulation of the flow over NACA0018 aerofoil without (Fig. 9, panel a) and with (Fig. 9, panel b) the acoustic term (Eq. (2.10)) active. The small separation bubble is visualized on the aerofoil's suction side by clipped negative values of $x$-velocity component. The bubble is clearly smaller in the case with acoustic excitation (Fig. 9b). The laminar-to-turbulent transition in separated boundary layer on aerofoil's suction side is visible by an intermittency function equal to unity (Fig. 9a, middle). The transition is followed by the boundary layer reattachment. The increased turbulent kinetic energy level is reported downstream of the transition point (Fig. 9a, bottom). In the case with acoustic excitation (Fig. 9b) the intermittency variable is activated earlier (Fig. 9b, middle) compared to the unexcited case (Fig. 9a, middle). It also results in earlier activation of the turbulent kinetic energy (Fig. 9b, bottom) compared to the unexcited case (Fig. 9a, bottom).

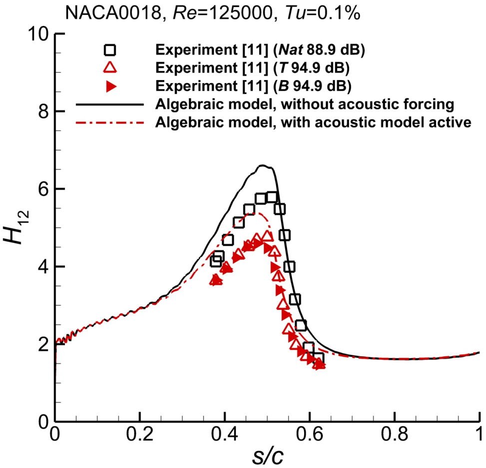

Fig. 10. Flow over NACA0018 aerofoil at $Re = 125\,000$, $Tu = 0.1\%$. Distribution of the shape factor on the aerofoil's suction side without and with acoustic excitation active.

Figure 10 shows comparison between measured and predicted by the algebraic model shape factor profiles on NACA0018 aerofoil's suction side in cases without and with acoustic excitation. In the experiment by Kurelek *et al.* [11] the *SPL* of the background noise in the unexcited case was equal to 88.9 dB (*Nat* symbol). Both the tonal ($T$) and broadband ($B$) excitation was imposed by an external loudspeaker at the *SPL* of 94.8 dB. The difference is 5.9 dB. Activation of acoustic perturbations resulted in shifting of the transition onset upstream. The present model reproduces well the unexcited and excited flow details. Numerically the separation point is reproduced somewhat too early in both cases (see also Fig. 11). This is due to a simple algebraic form of the $P_{\mathrm{KH}}$-production term (Eq. (2.8)). However, it can be seen that the proposed acoustic excitation component (Eq. (2.10)) functions well for the prediction of NACA0018 flow.

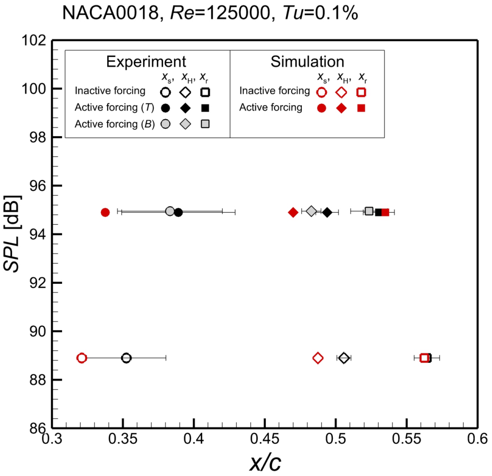

Fig. 11. Flow over NACA0018 aerofoil at $Re = 125\,000$, $Tu = 0.1\%$. Comparison between measured and predicted separation point ($x_s$), maximum shape factor location ($x_H$) and reattachment point ($x_r$) in cases without (88.5 dB) and with acoustic excitation (94.5 dB). In experiment, the symbols '*T*' and '*B*' denote the tonal and broadband forcing, respectively.

Figure 11 provides more quantitative information about measured and predicted by the algebraic model parameters i.e. separation point ($x_s$), maximum shape factor location ($x_H$) and reattachment point ($x_r$) in the cases without (88.5 dB) and with acoustic excitation (94.5 dB). The data are normalized by the aerofoil chord. The relative error between measured and predicted separation points is 8.8% and 13.2% in unexcited and excited flows, respectively. But one has to note a relatively large uncertainty level in measured values of separation. The predicted reattachment points are within the uncertainty limit of measured reattachment points in the two cases analysed here. Summing up, the algebraic intermittency model extended with the proposed acoustic excitation term (Eq. (2.10)) allows capturing the major effects of external acoustic excitation on transition in a separated boundary layer, with a satisfactory accuracy, which confirms the correctness of the assumptions made to model this phenomenon.

## 6. Summary

The simplified RANS-based method has been developed for taking into account the effect of acoustic forcing onto the laminar-to-turbulent transition inside a separated boundary layer. The modelling component (Eq. (2.10)) has been developed based on observation by Kurelek *et al.* [11] regarding an increase of the turbulent shear stress within a separated boundary layer under both tonal and broadband acoustic forcing. The model constant has been tuned based on the own flat plate experiment. The model calibration took into account reflections of acoustic waves at walls, reported in the present experiment. The model validation was performed using the reference experimental data by Kurelek *et al.* [11]. It should be emphasised that the present modification addresses only the effect of disturbances growth under external acoustic excitation, without taking into account the effect of varying the *SPL* level. The *SPL* effect seems important and might be the subject of a further study. Good quality results were obtained, proving applicability and reliability of the proposed modelling strategy for simulation of steady flows with active external acoustic forcing.

## Appendix A

Table A1 contains the coordinates of the test section. To prevent the flow separation, the leading edge of the flat plate (placed at $x = 0$, $y = -5$ mm) had an elliptical shape, with the semi-major axis equal to 38 mm, and minor axis equal to 10 mm. The plate thickness was equal to 10 mm.

Table A1. Coordinates of test section in mm.

| | | | | | | | | | |
|---|---|---|---|---|---|---|---|---|---|
| $x$ | 250 | 38 | 0 | 38 | 1415 | 0 | 90 | 190 | 240 |
| $y$ | $-10$ | $-10$ | $-5$ | 0 | 0 | 202 | 202 | 202 | 197 |
| $x$ | 265 | 290 | 315 | 340 | 370 | 390 | 440 | 490 | 600 |
| $y$ | 190 | 180 | 172 | 167 | 165 | 165 | 173 | 182 | 204 |
| $x$ | 700 | 800 | 900 | 1000 | 1103 | 1203 | 1303 | 1403 | 1415 |
| $y$ | 223 | 237 | 247 | 250 | 247 | 246 | 246 | 245 | 245 |

## Appendix B

Figure B1 shows a comparison of the shape factor profile along the flat plate surface (CUT flat plate) obtained on grids with 86 000 (coarse), 161 000 (basic) and 285 000 (fine) cells. The maximal values of $y^+$ were less than 0.6 on basic and fine meshes. The grid with 86 000 cells was coarsened with respect to 161 000 grid in the interior of the domain and in the near-wall region. On the coarse grid the value of $y^+$ parameter varied in the range 2.7–2.8. The comparison shows grid-independence of coarse and basic-grid results. Thus, the basic mesh was selected for calibration of the acoustic forcing term, discussed in Section 3.

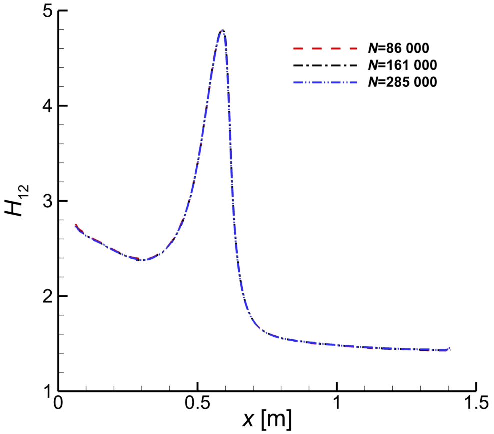

Fig. B1. Shape factor profile along the flat plate obtained on different density grids.

## Acknowledgements

The authors acknowledge the support from a research project funded by the Polish National Science Centre (Contract number DEC-2018/31/B/ST8/01717).

The authors acknowledge the Interdisciplinary Centre for Mathematical and Computational Modelling (ICM) at the University of Warsaw (Grant No. GB78-11) for granting the computational power for the numerical simulations.

## References

1. J. Slotnick, A. Khodadoust, J. Alonso, D. Darmofal, W. Gropp, E. Lurie, D. Mavriplis, *CFD Vision 2030 Study: A Path to Revolutionary Computational Aerosciences*, NASA/CR–2014-218178, 2014.
2. B.R. McAuliffe, M.I. Yaras, *Transition mechanisms in separation bubbles under low- and elevated freestream turbulence*, Journal of Turbomachinery, **132**, 011004/1-10, 2010.
3. W. Balzer, H.F. Fasel, *Numerical investigation of the role of free-stream turbulence in boundary-layer separation*, Journal of Fluid Mechanics, **801**, 289–321, 2016.
4. M. Wang, Z. Li, Ch. Yang, G. Han, S. Zhao, X. Lu, *Numerical investigations of the separated transitional flow over compressor blades with different loading distributions*, Aerospace Science and Technology, **106**, 106113/1-13, 2020.
5. D. Simoni, D. Lengani, M. Ubaldi, P. Zunino, M. Dellacasagrande, *Inspection of the dynamic properties of laminar separation bubbles: free-stream turbulence intensity effects for different Reynolds numbers*, Experiments in Fluids, **58**, 66, 1–14, 2017, doi: 10.1007/s00348-017-2353-7.

6. M.S. Istvan, S. Yarusevych, *Effects of free-stream turbulence intensity on transition in a laminar separation bubble formed over an airfoil*, Experiments in Fluids, **59**, 52, 1–21, 2018.
7. J. Serna, B.J. Lázaro, *The final stages of transition and the reattachment region in transitional separation bubbles,* Experiments in Fluids, **55**, 4, 2014, doi: 10.1007/s00348-014-1695-7.
8. K. Anand, K.T. Ganesh, *Characteristics of a separated flow past a semicircular leading-edge airfoil model under different imposed pressure gradient*, Proceedings of the Institution of Mechanical Engineers, Part G: Journal of Aerospace Engineering, 1–17, 2021.
9. R.E. Mayle, *The role of laminar-turbulent transition in gas turbine engines*, Journal of Turbomachinery, **113**, 509–537, 1991.
10. M. Dellacasagrande, R. Guida, D. Lengani, D. Simoni, M. Ubaldi, P. Zunino, *Correlations for the prediction of intermittency and turbulent spot production rate in separated flows*, Journal of Turbomachinery, **141**, 031003/1-8, 2019.
11. J.W. Kurelek, M. Kotsonis, S. Yarusevych, *Transition in a separation bubble under tonal and broadband acoustic excitation*, Journal of Fluid Mechanics, **853**, 1–36, 2018.
12. J.W. Kurelek, S. Yarusevych, M. Kotsonis, *Vortex merging in a laminar separation bubble under natural and forced conditions*, Physical Review Fluids, **4**, 063903/1-23, 2019.
13. S. Pröbsting, S. Yarusevych, Laminar separation bubble development on an airfoil emitting tonal noise, Journal of Fluid Mechanics, **780**, 167–191, 2015, doi: 10.1017/jfm.2015.427.
14. J. Michna, K. Rogowski, *Numerical study of the effect of the Reynolds number and the turbulence intensity on the performance of the NACA 0018 airfoil at the low Reynolds number regime*, Processes, **10**, 5, 1004, 2022.
15. E. Tangermann, M. Klein, *Numerical simulation of laminar separation on a NACA0018 airfoil in freestream turbulence*, in: AIAA Scitech 2020 Forum, American Institute of Aeronautics and Astronautics, 2020, doi: 10.2514/6.2020-2064.
16. R.A. Wahidi, S.M. Olçmen, *Suction effects on transitional bubbles*, Proceedings of the Institution of Mechanical Engineers, Part G, Journal of Aerospace Engineering, 1–14, 2021.
17. S. Kubacki, E. Dick, *An algebraic intermittency model for bypass transition in turbomachinery flows,* International Journal of Heat and Fluid Flow, **58**, 68–83, 2016.
18. S. Kubacki, E. Dick, *An algebraic intermittency model for bypass, separation-induced and wake-induced transition*, International Journal of Heat and Fluid Flow, **62**, 344–361, 2016.
19. K. Nering, K. Rup, *An improved algebraic model for by-pass tranistion for calulation of tranistional flow in pipe and parallel-plate channels*, Thermal Science, **23**, 4, 1123–1131, 2019.
20. K. Nering, K. Rup, *Modified algebraic model of laminar-turbulent transition for internal flows*, International Journal of Numerical Methods for Heat and Fluid Flow, **30**, 4, 1743–1753, 2020.
21. J. Holman, J. Fürst, *Coupling the algebraic model of bypass transition with EARSM model of turbulence* Advances in Computational Mathematics, **45**, 1977–1992, 2019.
22. J. Holman, J. Fürst, *Numerical simulation of separation induced laminar to turbulent transition over an airfoil* Journal of Computational and Applied Mathematics, **394**, 113530/1-15, 2021.

23. P. Louda, J. Přihoda, K. Kozel, *Transition modelling on separated flow in turbine cascade* in: Proceedings Topical Problems of Fluid Mechanics, D. Šimurda, T. Bodnár [eds.], Prague, pp. 211–220, 2017.
24. D.C. Wilcox, *Formulation of the k-ω turbulence model revisited*, AIAA Journal, **46**, 2823–2838, 2008.
25. D.K. Walters, D. Cokljat, *A three-equation eddy-viscosity model for Reynolds-averaged Navier–Stokes simulations of transitional flow*, Journal of Fluids Engineering, **130**, 121401/1-14, 2008.
26. S. Kubacki, D. Simoni, D. Lengani, M. Dellacasagrande, E. Dick, *Extension of an algebraic intermittency model for better prediction of transition in separated layers under strong free-stream turbulence*, International Journal of Heat and Fluid Flow, **92**, 1–16, 2021, doi: 10.1016/j.ijheatfluidflow.2021.108860.
27. F.R. Menter, P.E. Smirnov, T. Liu, R.A. Avancha, *One-equation local correlation-based transition model*, Flow Turbulence and Combustion, **95**, 583–619, 2015.
28. S. Kubacki, D. Simoni, D. Lengani, M.E. Dick, *An Extended version of an algebraic intermittency model for prediction of separation-induced transition at elevated free-stream turbulence level*, International Journal of Turbomachinery, Propulsion and Power, **5**, 4, 28, 2020.
29. V. Sokolenko, W. Elsner, A. Dróżdż, R. Gnatowska, Z. Rarata, S. Kubacki, *Experimental analysis of the impact of an acoustic excitation on a separated boundary layer behaviour*, Journal of Physics: Conference Series, **2367**, 012021, doi: 10.1088/1742-6596/2367/1/012021, 2022.
30. L. Zhou, Z. Gao, Y. Du, *Flow-dependent DDES/*$\gamma - \bar{Re}_{\theta t}$ *coupling model for the simulation of separated transitional flow*, Aerospace Science and Technology, **87**, 389–403, 2019.
31. M. Drela, M.B. Giles, *Viscous-in viscid analysis of transonic and low Reynolds number airfoils,* AIAA Journal, **25**, 10, 1347–1355, 1986.
32. D. Lengani, D. Simoni, M. Ubaldi, P. Zunino, F. Bertini, *Experimental study of free-stream turbulence induced transition in an adverse pressure gradient*, Experimental Thermal Fluid Science, **84**, 18–27, 2017.
33. J.W. Kurelek, B.A. Tuna, S. Yarusevych, M. Kotsonis, *Three-dimensional development of coherent structures in a two-dimensional laminar separation bubble*, AIAA Journal, **59**, 7, 1–13, 2020.
34. C. Gramespacher, H. Albiez, M. Stripf, H.-J. Bauer, *The generation of grid turbulence with continuously adjustable intensity and length scales*, Experiments in Fluids, **60**, 85, 1–15, 2019.

*Received June 24, 2023; revised version August 10, 2023.*